INL/JOU-24-81743-Revision-1

Fast-charging lithium-ion batteries: Synergy of carbon nanotubes and laser ablation

February 2025

Tanvir R Tanim, Saiful Islam, Eric J Dufek, Bianca Yi Wen Mak, Michael C Evans, Avtar Singh, Alison R. Dunlop, Peter J. Weddle, Ryan Tancin, Stephen E. Trask, Andrew M. Colclasure, Donal P. Finegan, Kandler Smith, Andrew N. Jansen, Kevin L Gering, ZhenZhen Yang, Geetika Vennam

Changing the World's Energy Future

Idaho National Laboratory

INL is a U.S. Department of Energy National Laboratory operated by Battelle Energy Alliance, LLC

INL/JOU-24-81743-Revision-1

Fast-charging lithium-ion batteries: Synergy of carbon nanotubes and laser ablation

Tanvir R Tanim, Saiful Islam, Eric J Dufek, Bianca Yi Wen Mak, Michael C Evans, Avtar Singh, Alison R. Dunlop, Peter J. Weddle, Ryan Tancin, Stephen E. Trask, Andrew M. Colclasure, Donal P. Finegan, Kandler Smith, Andrew N. Jansen, Kevin L Gering, ZhenZhen Yang, Geetika Vennam

February 2025

Idaho National Laboratory
Idaho Falls, Idaho 83415

http://www.inl.gov

Prepared for the
U.S. Department of Energy
Under DOE Idaho Operations Office
Contract DE-AC07-05ID14517

Fast-Charging Lithium-Ion Batteries: Synergy of Carbon Nanotubes and Laser Ablation

Geetika Vennam[1], Avtar Singh[2], Alison R. Dunlop[3], Saiful Islam[1], Peter J. Weddle[2] , Bianca Yi Wen Mak[1], Ryan Tancin[2], Michael C. Evans[1], Stephen E. Trask[3], Eric J Dufek[1], Andrew M. Colclasure[2], Donal P. Finegan[2] , Kandler Smith[2], Andrew N. Jansen[3], Kevin L. Gering[1], ZhenZhen Yang[3], and Tanvir R. Tanim[1,*]

[1] Energy Storage and Electric Transportation Department, Idaho National Laboratory, Idaho Falls, ID, 83415, USA.

[2] Energy Conversion and Storage Systems Center, National Renewable Energy Laboratory, Golden, CO, 80401, USA

[3] Chemical Sciences and Engineering Division, Argonne National Laboratory, Lemont, IL, 60439, USA

Correspondence*: tanvir.tanim@inl.gov

Highlights

- The study examines the combined effects of SWCNT in cathode and LA in anode.
- SWCNTs and LA improve 10–15 min fast charging performance in LiBs.
- SWCNTs raise 5C charge acceptance by 13.1 %, lowering polarization.
- SWCNT + 12% LA reduce Li plating, maintaining ~85 % capacity at 5C after 800 cycles.
- 15 % LA cells fade >30 % due to LLI and LAM in NE and PE, respectively.

Abstract

Advancing lithium-ion battery (LiB) technology to achieve 10–15-minute extreme fast charging (XFC) while maintaining high energy density and longevity poses a significant challenge. Addressing Li-plating is crucial, as it depletes usable Li, causing deterioration and safety issues. This study explores a holistic approach incorporating Single-Wall Carbon Nanotubes (SWCNTs) and Laser Ablation (LA) to mitigate Li-plating while maintaining high charge acceptance under 10–15-minute XFC. SWCNTs enhance the electrical conductivity and mechanical integrity of the positive electrode (PE), reducing overall cell overpotential at high charging rates. Concurrently, LA is applied to negative electrodes (NE) to reduce tortuosity of ion-diffusion pathways and increase surface wettability, improving Li-ion transport. Combining SWCNTs in the PE and LA on the NE, our experimental findings demonstrate a significant reduction in Li-plating and maintained high charge acceptance of ~84.33% after 800 5C (12 min) charge cycles for cells having PE with ~3.3 mAh cm^{-2} and NE with 3.9 mAh cm^{-2} loadings. This study highlights the potential of combining SWCNTs and LA to address Li-plating in LiBs and opens new avenues for designing battery systems capable of achieving 10–15-minute XFC.

Keywords: Lithium plating, Fast-charging, Lithium-ion batteries, Laser ablation, Single-wall carbon nano tubes.

1 Introduction

Enabling extreme fast charging (XFC) technology in energy-optimized LiBs—i.e., recharging within 10 to 15 minutes—represents a substantial advancement in the field of battery technology. This feature is widely sought after by different LiB applications driven by end user sentiment [1–3]. Achieving a 10- to 15-minute XFC requires a charging rate ranging from 4C to 6C, which has been demonstrated in research and development (R&D) cells. These cells typically use low to moderately loaded electrode designs (≤3 mAh cm-2), achieved through integrating diverse solution strategies [4]. However, the aspiration to enable XFC in cells with higher energy densities (≥4 mAh cm-2), with the aim to develop cells that can maintain desired driving ranges at lower costs, necessitates further advancements.

In recent years, there has been extensive characterization and documentation of performance bottlenecks and degradation mechanisms linked to XFC [3,5–13]. Polarization losses originating within electrodes and sluggish Li+ transport in the electrolyte have been identified as a key hindrance to fast charging. These factors lead to voltage losses, driving the negative electrode (NE) potential towards the Li-plating regime, and adversely affecting charge acceptance [8,14]. Furthermore, these polarization issues are exacerbated when increasing electrode loading [10].

Recent studies have introduced new approaches to mitigate fast-charge challenges, encompassing advancements from materials-to-electrode design and introducing novel charging protocols [4,15–24]. For example, Tanim et al. highlighted that lithium nickel manganese cobalt oxide (NMC) with a higher nickel content (NMC811) outperforms its lower nickel counterpart (NMC532) under XFC scenarios due to NMC811's increased electronic conductivity [15,16]. These features notably decrease the overall overpotential at elevated charging rates. Usseglio-Viretta et al. optimized electrode compositions to enhance Li+ transport behavior and minimize overpotential by reducing positive electrode (PE) impedance, electrode tortuosity, and PE thickness through optimized carbon-binder domain [17]. Introducing dual-layer NEs, with smaller particles close to the separator and larger particles near the current collector, has been shown to reduce transport-related polarization losses, thereby enhancing XFC capabilities [4]. Employing a more porous separator has also been effective in reducing polarization losses [4]. Furthermore, innovative electrolytes are being actively investigated to enhance Li+ transport for XFC [14,23]. These formulations include replacing carbonate-based solvents with alternative solvents such as ethers or nitriles [18–23], with some studies arguing for multi-solvent and mixed salt systems that offer a balanced set of properties conducive to XFC [23]. Additionally, replacing the LiPF6 salt with alternatives like LiFSI has been found to enhance Li+ transport, showing promise for future advancements in fast-charge technology [24].

Previous research has indicated that at higher rates, the PE predominantly contributes to cell polarization, highlighting the importance of minimizing impedance and transport-related losses specifically at the PE [8,25]. To address this, various strategies have been proposed, including material selection such as enhancing nickel content in the NMC PE, utilizing radially or oriented single crystal primary particles, and employing dual-layer electrode designs [4,8,15]. Additionally, electrodes with carbon nanotubes (CNTs) have been used to enhance conductivity at the electrode-level and has been a viable approach in mitigating impedance polarization. The reduced electrode-

level resistance is due to the exceptional electron transport properties of CNTs, which facilitate faster electron movement and subsequently reduces the necessary carbon-binder phase volume fraction of which can increase the electrolyte tortuosity [26]. Incorporating CNTs into electrodes was shown to significantly enhance the cycle life and rate capability of LiBs [27–29]. However, achieving a uniform and stable distribution of CNTs within the electrode matrix remains challenging [30,31].

Laser ablation (LA) is another way to reduce cell polarization at higher rates and improve the fast-charge cycling performance. Recently, research has shown that laser patterning the NE or both the electrodes improves the rate capability, improves electrode wetting and reduces the risk of Li-plating during fast charging [32–37].

Incorporating multiple solution strategies is important to facilitate XFC in LiBs [4,14,38]. Tanim et al. investigated integrating six XFC strategies (high-Ni PE chemistry, reduced carbon binder domain in the PE, a dual-layer NE design, a higher porosity separator, using advanced electrolytes and innovative charging protocols) in a moderate-loading cell design with an ~3 mAh cm-2 NE, showcased successful 6C (10 min) XFC without plating for up to 600 cycles [4]. Wang et al. investigated 15 min fast charging of energy-dense batteries (3.4 mAh cm-2) by combining material-agnostic approach based on asymmetric temperature modulation with a thermally stable dual-salt electrolyte and larger porosity NE for improved ion transport to achieve charging of a 265 Wh kg−1 battery to 75% (or 70%) state of charge for more than 900 (or 2,000) cycles [38]. Dasgupta et al. showed notable enhancements in the cycle life of moderate loading multilayer pouch cells (>2 mAh cm-2) by using laser-patterned graphite NE with a loading of 3 mAh cm-2. These cells retained 91% and 86% of their capacity after 600 fast charge cycles at rates of 4C and 6C, respectively [35]. Babkin et al. investigated the impact of different carbon additives on the rate capability of LFP PEs [39]. The LFP PE incorporating SWCNTs exhibited significantly superior high-rate capability (>3C) as compared to electrodes with double-wall or multi-wall carbon nanotubes. However, it is imperative to extend XFC performance to higher-loading cells (i.e., ≥ 4 mAh cm-2), which have greater industrial and commercial relevance. Therefore, existing solution strategies must be improved or new strategies implemented to reduce polarization losses during fast charging of higher-loading electrodes.

This article demonstrates the ability of SWCNTs in PEs and LA of NEs to mitigate cell polarization losses to facilitate Li-plating-free XFC in high-loading cells. Additionally, we explore the effect of LA on high-loading NEs and the effects of LA material removal. An advanced electrolyte and a high-porosity separator are used in single-layer pouch cells (SLPCs) to demonstrate the feasibility of achieving XFC at up to 5C rates (12 min) for hundreds of cycles. Combined, these approaches not only support XFC but mitigate critical degradation pathways such as Li-plating, enhancing overall performance and longevity

2 Methodology

2.1 SWCNTs in PEs

Electrodes with CNTs have exhibited superior cycle performance as compared to electrodes using traditional conductive additives like Super-P conductive carbon [26–28,40]. These performance improvements are largely attributed to a more uniform electronic conductivity provided by the CNTs, which effectively reduces internal resistance and suppresses polarization during high-rate charging and discharging, as evidenced by evaluations conducted at 5C [26,27]. For instance, electrochemical tests performed on half-cell coin cells comprising of NCM811 PE active material, poly (vinylidene fluoride) (PVDF) binder, and CNTs in a 97:2:1 wt. ratio revealed significantly enhanced electrochemical properties [27].

Further emphasizing the benefits of SWCNTs, Choi et al. [27] reported that NMC PEs containing SWCNTs achieved 92.8% capacity retention after 100 cycles at a 5C rate in coin cells, showcasing considerable improvement in cycling performance under fast-charge conditions. Another study [28] investigated the effects of ozonated SWCNTs on high-loading (30 mg cm-2 or higher) dry-processed NCM811 coin cells. The results showed that the enhanced affinity of NCM811 particles to form denser microstructures within the PE composite, coupled with protection against unwanted side reactions at the cathode-electrolyte interface (CEI), ultimately resulted in reduced microcracking in NCM811 particles during cycling.

While the SWCNT one-dimensional structure and superior electrical conductivity enhances electron transport and mechanical resilience within the PE, facilitating better integrity throughout frequent expansion and contraction cycles [40], existing research predominantly focuses on coin-cell discharge performance with relatively short cycle-life evaluations. There remains a significant gap in the literature concerning the use of SWCNTs under XFC conditions (4C-6C) and their long-term performance in larger scale SLPCs. These gaps highlight the need for more comprehensive studies that examine the effects of SWCNTs under varied operational conditions, particularly those that simulate real-world applications where fast charging and high durability are critical

2.2 Laser Ablation

Introducing strategic microstructural features into battery electrodes, such as those achieved using femtosecond LA, have been shown to improve both electrolyte wetting and cell fast-charge performance [32,35,37]. LA has been reported to reduce electrode Li+-transport tortuosity through the electrode's thickness, allowing for higher C-rates before the onset of Li-plating.

Figure 1 shows the predicted cell performance improvements expected in LA cells as compared to non-ablated cells. For the cell with a non-ablated NE, a previously developed and calibrated pseudo-2D (P2D), macro-homogeneous, Newman-type, electrochemical model is employed [41]. To simulate the effects of LA, a pseudo-4D (P4D) model is developed and calibrated in COMSOL Multiphysics. The P4D model's increased dimensionality captures the effects of the 3D laser-pattern geometry [42]. Schematic illustrations and calibration plots for both the P2D (non-ablated) and P4D (laser-ablated) models are provided in Supplemental Sections S 1, and S 2, while details of the LA process, parameters and LA geometry are available in Supplemental Section S 3 and Table T 1.

Both the P2D and P4D models capture the full-cell performance response of graphite without SWCNT vs NMC811 with SWCNT using Gen2 + 2 wt.% FEC electrolyte, later used for experimental validation. Supplemental Table T 2 lists the model parameters for all cell builds. The microstructure properties were determined using National Renewable Energy Laboratory's (NREL's) MATBOX tool [43], while the electrolyte properties are obtained from the Idaho National Laboratory's (INL's) Advanced Electrolyte Model (AEM) [44]. Using the data obtained from the AEM, the electrolyte properties are fit with polynomials (see Supplemental Table T 3). A constant-current—constant-voltage (CC-CV) charging protocol is considered at 5C C-rate that achieved 80% capacity in 10 min

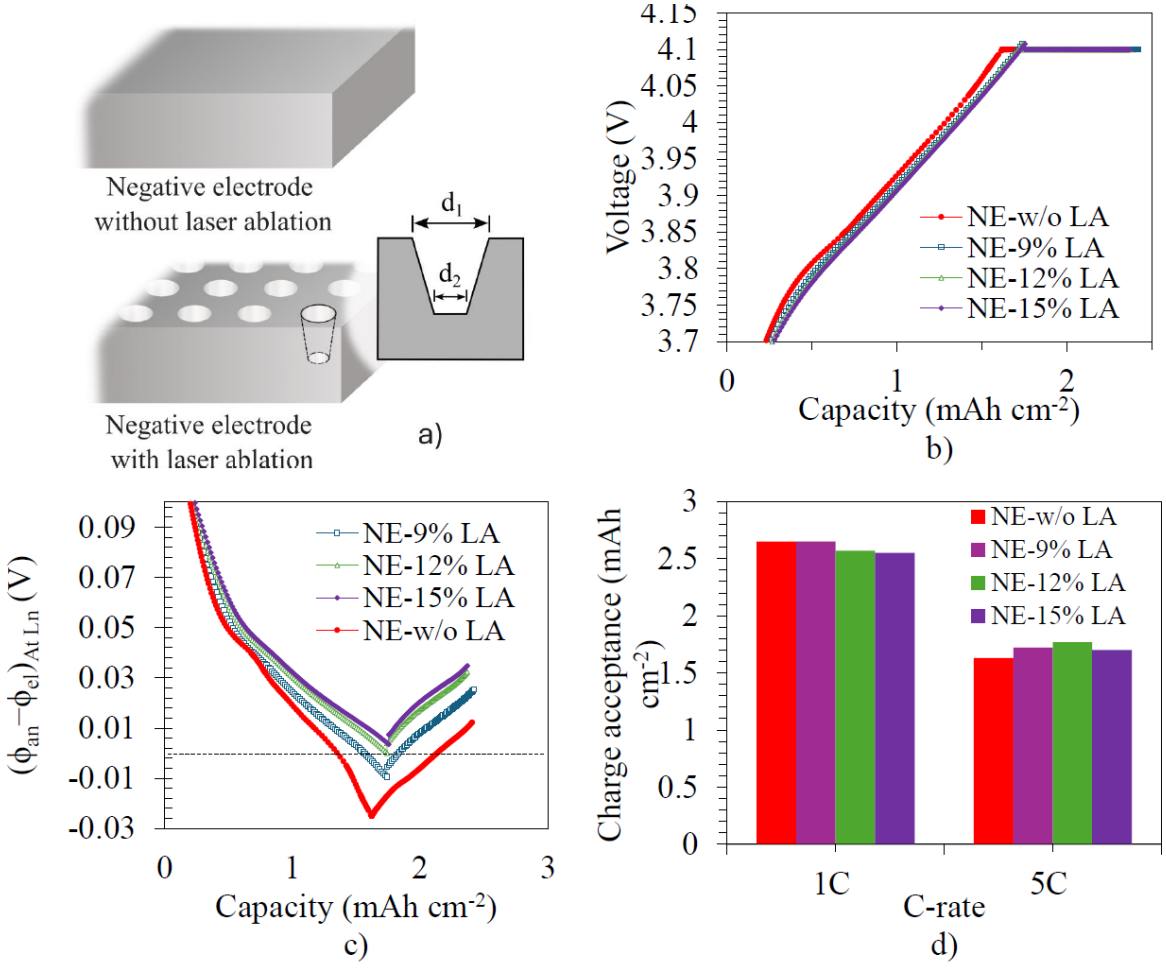

Figure 1. (a) Schematic illustration of negative electrode without and with laser-ablated geometry, b) Comparison of predicted beginning-of-life (BOL) 5C CC-CV terminal voltage response, (c) predicted minimum plating potential evolution for cells with non-ablated and 9%, 12%, and 15% laser-ablated NEs, and (d) BOL rate performance experimental data.

Figure 1b-c illustrates the model-predicted terminal voltage and plating potential with respect to capacity. The plots include responses for the non-ablated and the LA NE designs, which have approximately (9%, 12%, and 15% laser-ablated mass removal). All laser-ablated NEs were from the same slurry batch and same coating. The NE sheets started at the same loading as each other,

but each sheet had a different extent of LA. This caused the loading to decrease as the percentage LA increased. The LA NEs had the following loadings: with 9% LA at 4.03 mAh cm-2, 12% LA at 3.85 mAh cm-2, and 15% LA at 3.75 mAh cm-2. The non-laser ablated NE was from a different slurry batch, but same formulation. The non-laser ablated NE had a loading of 4.04 mAh cm-2, similar to that of the 9% LA NE. At a relatively slow 1C C-rate (Figure 1d), cells with the non-ablated NE is predicted to achieve capacities of 2.65 mAh cm-2 at the end of CC condition. In contrast, cells with a laser-ablated NE are predicted to achieve capacities of 2.65 mAh cm-2, 2.57 mAh cm-2, and 2.55 mAh cm-2, for 9%, 12%, and 15% LA, respectively, which is proportional to the electrode loadings at the end of CC condition.

However, at a relatively fast 5C C-rate (Figure 1d), the non-ablated NE cell is predicted to reach capacities of 1.63 mAh cm-2, while the laser-ablated NE cells are predicted to have enhanced capacities of 1.72 mAh cm-2, 1.77 mAh cm-2, and 1.70 mAh cm-2 for 9%, 12%, and 15% LA, respectively at the end of CC condition. These predicted increases represent capacity improvements of 5.5%, 8.5%, and 4.3% for each ablation level, underscoring the benefits of laser-ablated designs at higher charging rates. Figure 1c further reveals that the predicted minimum plating potential at the end of the CC mode for the 12% and 15% LA cases are above 0 V (0.076 mV and 3.48 mV, respectively), unlike the non-ablated NE. This suggests enhanced resilience to Li-plating in the laser-ablated cases, which is crucial for minimizing loss-of-lithium-inventory (LLI)

2.3 Experimental

2.3.1 Cell design

The Cell Analysis, Modeling and Prototyping (CAMP) Facility at Argonne National Laboratory (Argonne) fabricated sixteen SLPCxx3450-format cells with six distinct design variants, detailed in Table 1. These designs were influenced by findings from earlier studies [4,8,14,17,17,23,32], and reports on the beneficial effects of SWCNT and LA. The key focus of the present study is evaluating XFC performance improvements of SWCNTs in the PE and LA in the NE using well designed SLPCs during extended cycling

Table 1. Cell-build information

SLPC design	PE, mAh cm^{-2}	NE, mAh cm^{-2}	C/10 N:P	Comment
D1, PE-w/o SWCNT	3.12, No SWCNT	3.77, No LA	1.21	Evaluates the effects of SWCNT.
D2, PE-w/ SWCNT	3.08, SWCNT	3.70, No LA	1.20	
D3, NE-w/o LA	3.39, SWCNT	4.04, No LA	1.19	Evaluated the combined effects of SWCNT in PE and LA in NE. D3 is the baseline for D4, D5, and D6.
D4, NE-9% LA	3.36, SWCNT	4.03, 9% LA	1.20	
D5, NE-12% LA	3.27, SWCNT	3.85, 12% LA	1.18	
D6, NE-15% LA	3.23, SWCNT	3.75, 15% LA	1.16	

D1=Design 1, D2=Design 2, D3=Design 3, D4=Design 4, D5=Design 5, D6=Design 6.

The PE designs include a PE without SWCNT (D1) and PEs with 0.05 wt% Tuball SWCNT (D2-D6). For the NE, the designs include no LA (D1-D3) and electrodes with approximately 9%, 12%, and 15% LA (D4-D6). The supplemental information S 3 describes the LA process with relevant parameters. Table 1 outlines the cell builds with corresponding electrodes and loading

information, ensuring an N:P ratio between 1.16 and 1.21 for all cells. The D1 and the D2 design cells are used to assess the impact of SWCNT. Designs D3 through D6 are used to evaluate the combined effects of SWCNT in the PE and LA in the NE. Detailed cell design parameters are provided in Table T 4-Table T 9.

The cells were initially formed, degassed, underwent 1 kHz impedance measurements, and a final capacity check at the CAMP facility before being transported to INL for cycle-life evaluation. At INL, the design of experiments was developed, followed by comprehensive cycle-life studies and aging-mode analyses.

At INL, initial evaluations were conducted to measure the BOL cell variability. Each cell was secured using fixtures applying pressures between 15–30 kPa. The entire fixture was placed in a thermal chamber (specific models used were TestEquity 1007C, Espec, or Associated Environmental System Chambers) and maintained at a consistent temperature of 30 ± 1 ◦C. All charging and discharging tests were automated using a MACCOR Series 4000 system. For additional details on the fixturing process, see reference [45]. Electrochemical impedance spectroscopy (EIS) measurements were performed using a Solartron 1287 potentiostat and a Model 1260 analyzer. The Supplemental Table T 10 presents the average values and the 1σ standard deviation for various metrics such as mass, open circuit voltage, and high-frequency impedance of the as-received 16 cells. These tests show a tight spread except for the D1 cells; measured capacities at C/20 and C/3 also shown to have little cell-to-cell variation. All 16 cells, from D1-D6, underwent initial BOL testing, encompassing assessments such as static-capacity evaluation test (SCT), C/20 charge/discharge cycle tests, EV hybrid pulse-power characterization (HPPC) [46], and EIS tests. Supplemental Table T 11 and Table T 12 provides a more-detailed breakdown of the BOL testing procedures.

Following BOL testing, 8 cells: one cell from each D2-D6 and 3 cells from D1 underwent a rate capability test (RCT). This test involved CC-CV charging at various C-rates based on the capacity at C/3 from the BOL SCT. The charging rates ranged from 0.5C up to 7C, with a cutoff voltage set at 4.1V. After each charging step in the RCT, a 30-minute rest period was implemented to gather cell impedance and transport polarization data. The cells were then discharged at C/3 to 3V, followed by another 30-min rest before the next charging cycle, continuing until the 7C charge rate was completed.

Impedance polarization, which includes ohmic and charge-transfer impedances, was determined by the immediate voltage drop (within approximately 12 ms) following each charging step [14,45]. Transport polarization, reflecting the combined Li-ion transport-related losses in both the liquid and solid phases, was determined from the voltage drop observed between 12 ms to 30 min [14,45].

Additionally, the coulombic efficiency (CE) and the rate of voltage change (dV/dt) during rest periods after charging were calculated for various charge-discharge steps throughout the RCT tests. The insights derived from impedance and transport-polarization, along with CE and dV/dt, can be used to understand underlying mechanisms occurring during fast-charge [8,14,17,45,47,48]. Based on the findings from these electrochemical measurements, a 5C CC-CV charging protocol was established at 30 °C. Under this protocol, 8 cells (2 cells each from D3-D6) were charged at 5C up to 4.1V, followed by CV charging at 4.1V until a total charging time of 12 min (CC + CV) was reached. For cycling, the following protocol was adopted: cells were discharged at C/3, rested for 30 minutes, and then charged to 4.1V using the 5C CC-CV method with a 30-minute rest after charging. This cycle was repeated for each cell from D3-D6 over 800 cycles, with reference

performance tests (RPTs) being conducted at specified cycle intervals as detailed in Supplemental Table T 13. The RPTs included a slow-rate C/20 charge-discharge test between 3 and 4.1V and an EIS test at 3.8V (Table T 11 and Table T 12), both of which were used to assess the cell's state of health

3 Results

3.1 BOL performance with and without SWCNT

Figure 2 shows the comparison between D1 and D2, identified as PE-w/o SWCNT and PE-w/ SWCNT, respectively. Figure 2a, b shows that cell with SWCNT in the PE, showed distinct improvement in impedance and transport polarizations during XFC conditions. Unlike the PE-w/ SWCNT condition, the cell without SWCNT in the PE, also exhibits a plateau-like in the transport polarization (Figure 2b) behavior after approximately 4C, which has previously been attributed to Li-plating [49].

The Nyquist plot in Figure 2c shows that the inclusion of SWCNT marginally enhances the ohmic performance. However, the majority of the impedance polarization originates from the charge-transfer impedance, as indicated by the mid-frequency depressed semi-circle. Figure 2d illustrates that the D2 cells significantly outperformed the D1 cells in terms of charge acceptance at higher C-rates (>1C). Specifically, the D2 cells achieved an impressive 83.7% charge acceptance at a 5C rate over a 12-min charging period within a 3–4.1V voltage window. In comparison, the D1 cells managed only 70.5% charge acceptance under the same conditions, marking a substantial decrease of 13.1% as detailed in Supplemental Figure S 4d. Charge acceptance is defined as the ratio of the charge stored by the battery during a CC-CV charging event to its nominal discharge (or rated) capacity @ C/3, multiplied by 100 to express it as a percentage.

Unlike the transport polarization curves (Figure 2b), the CE and dV/dt curves (Figure S 4a-c) did not show any significant drops or sharp peaks, indicating an absence of Li-plating at high C-rates (>3C) for both cell types (D1 and D2). As described by Vennam et al., this behavior is common, as not all signatures are indicative of Li-plating [49]. Thus, it is standard practice to apply multi-signal analysis to accurately detect Li-plating

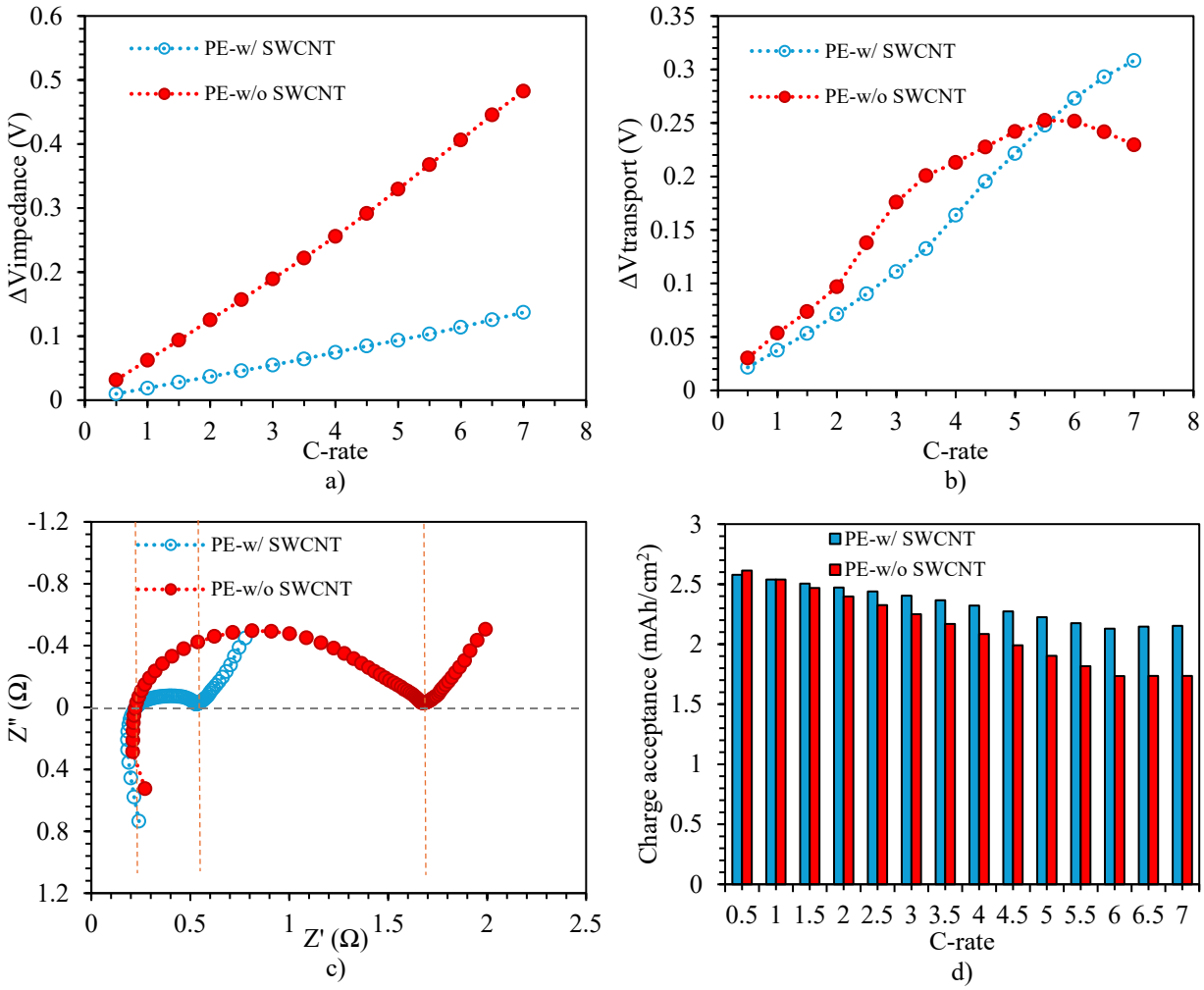

Figure 2. a) and b) BOL impedance and transport polarizations, obtained from RCTs for with and without SWCNT (average of 3 cells) designs, respectively c) BOL EIS for with and without SWCNT (average of 3 cells) designs, d) charge acceptance with and without SWCNT designs at 0.5C-7C in mAh.cm^{-2}.

3.2 BOL performance with SWCNTs, and without and with LA

Incorporating SWCNTs into the PE significantly enhanced cell performance at the macroscale, as discussed in Section 3.1. Figure S 5 contrasts the electrochemical characteristics of D2 with D3. Despite D3 featuring slightly higher loading and lacking LA in the negative electrode (NE), it includes SWCNT in the PE, similar to D2. Figure S 5a reveals that the CC-CV normalized areal charge acceptance of D3 is superior across all tested C-rates (0.5C-7C). However, at 5C, D3 exhibits a lower normalized recharge percentage and a drop in CE (Figure S 5b,c), suggesting Li-plating, although the recharge percentage remains robustly above 80% at this high C-rate. Consequently, the high loading and SWCNT in D3 enhances its areal capacity, establishing it as the baseline for subsequent comparisons with other designs (D4-D6) that incorporate NE with LA.

Comparative analysis of the LA effects (D4-D6) to those without LA (D3) reveals notable improvements. All Designs (D3-D6) contain SWCNT in the PE, enhancing the baseline PE

electrical conductivity. As shown in Figure 3a, adding LA significantly enhances impedance polarization up to a 3C rate, achieving similar improvements to those observed with SWCNT in PE (D2). Furthermore, the combined effect of SWCNT and LA eliminates any distinct transport polarization plateau up to 7C, as seen in Figure 3b. This is evidenced by transport polarization improvements of up to 40% (Supplemental Figure S 6a), with the 12% LA showing optimal performance.

Figure 3c, and d highlights that LA significantly enhances both CE and charge acceptance. Specifically, treatments with 12% LA (D5) and 15% LA (D6) achieve the highest CC-CV charge acceptance rates of 84.6% and 85.1%, respectively, at a 5C rate within a 12-minute charge period. These values surpass the 82.2% charge acceptance of baseline cells without LA (D3), showing a 3.38% increase in charge acceptance despite lower overall anode loading.

Additional dV/dt analysis (Supplemental Figure S 6d, e) supports the superior performance of cells treated with 12% and 15% LA, as they exhibit no dV/dt shoulders—an indicator of effective Li-plating suppression. Although the model (Figure 1c) predicts that cells with 9% LA (D4) outperform those without LA (D3), the CE curves (Figure 3c) beyond 5C do not show a steep drop for D3. This discrepancy may stem from the model's predictive accuracy, which appears most reliable up to 5C, where CE curves for D3 and D4 are comparable.

However, the partially laser-ablated electrode microstructure (D4) could introduce localized variations in current density and ion transport that are not fully captured by the model. These variations may lead to increased side reactions or localized lithium plating at very high rates (>5C), thus reducing CE. Other data, such as Figure 3d and Supplemental Figure S 6b and c, indicate lower overall charge acceptance in D3 relative to D4, with noticeable Li-plating shoulders appearing at 5C in D3 but only at 5.5C in D4. Consequently, 9% LA (D4) does indeed perform better than the baseline (D3), and it would be premature to conclude that D3 is superior based solely on CE trends observed beyond 5C.

To justify the study design, it is crucial to clarify the decision-making process regarding the cycling protocols. Initial electrochemical tests demonstrated that D3 provided superior areal charge acceptance, leading to the decision not to study cycle-life in D1 and D2. This was based on preliminary insights indicating that cycling these designs would not yield additional benefits but rather replicate known limitations like reduced areal charge acceptance and increased Li-plating susceptibility. Thus, the focus of the cycling study shifted to evaluating D3-D6 using a 5C-12-min CC-CV charging protocol. This protocol was selected due to its challenging, yet practical, approach for assessing high-rate conditions, allowing the team to examine the charge acceptance capabilities, improved polarization and the efficiency of Li-plating suppression mechanisms (Figure 3c,d, Figure S 6) within a realistic timeframe suitable for high-performance applications

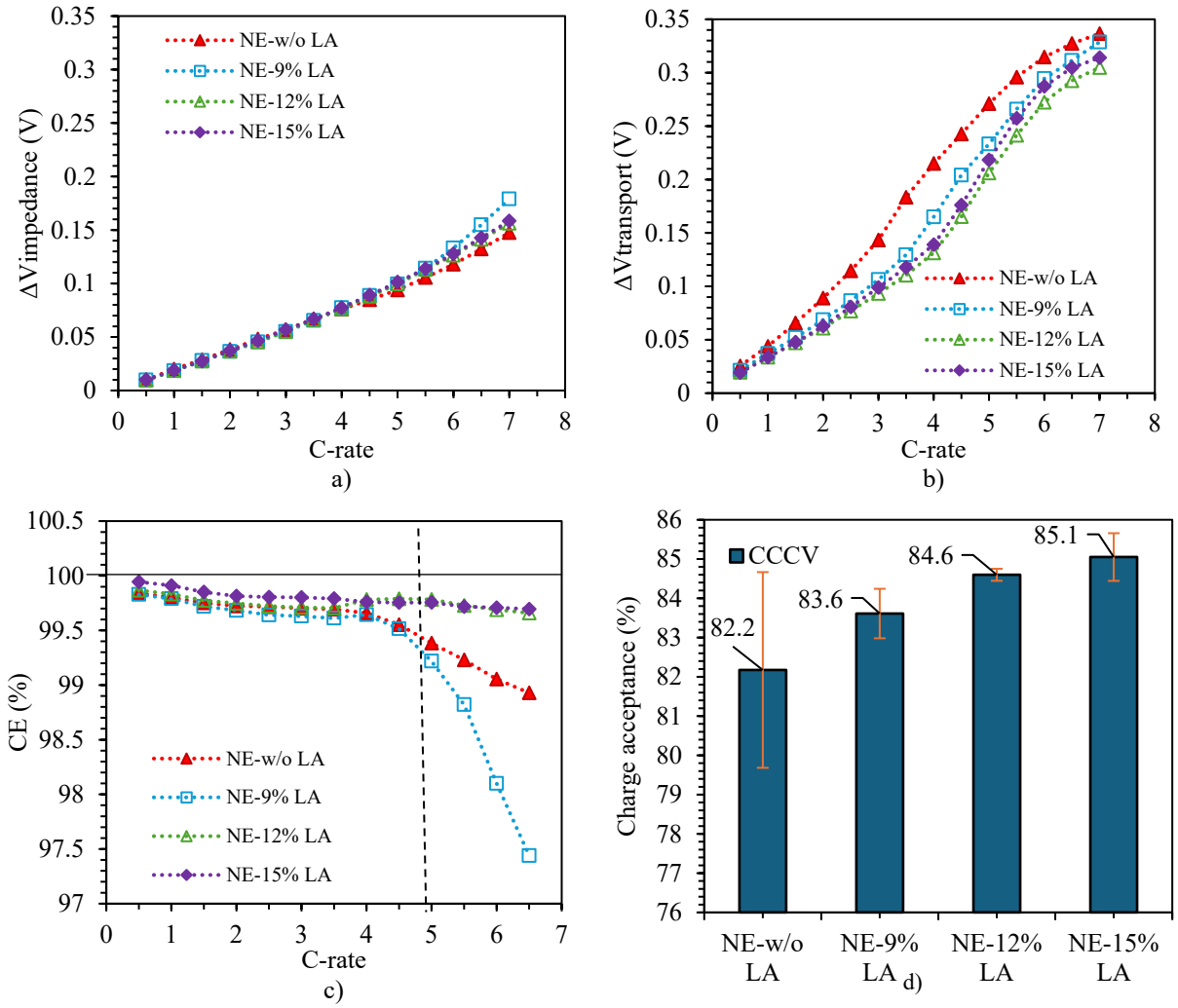

Figure 3. a) and b) BOL impedance and transport polarizations, obtained from RCTs for with and without LA designs, c) CE with and without LA designs in % and d) 5C CC-CV Ah based charge acceptance (%) from 3-4.1V with and without LA designs.

3.3 Cycle life performance

In this study, we employed a 5C-12 min CC-CV charging protocol to test cells from D3-D6 up to 800 cycles, analyzing the cycle life performance at these fast-charge rates coupled with C/3 discharge rates. The collected CC-CV cycle life testing data are detailed in Figure 4, Figure 5 and Supplemental Figure S 7, which illustrate the cycle-by-cycle (CBC) electrochemical analysis results.

Figure 4a) reveals the normalized CC-CV recharge percentages across the cycle number, where cells treated with 15% LA (D6) and those without LA (D3) exhibited notably poorer performance as compared to the 9% (D4) and 12% (D5) LA cells; the charge acceptance for the D6 and D3 cells decreased to 77.32% after 500 cycles (for both designs) and further deteriorated to 66.66% and 77.11%, respectively by 800 cycles. In contrast, cells with 9% and 12% LA treatments maintained higher charge acceptance rates of 86.1% and 89.6% after 500 cycles, which slightly decreased to 80.98% and 84.33% by the end of 800 cycles, respectively. Supplemental Figure S

7a displays the CBC charge acceptance in mAh cm-², with the 12% LA cells at 2.0 mAh cm-² and the 15% LA cells at 1.58 mAh cm-².

Figure 4b presents the end-of-charge (EOCV) rest voltages, taken after a 30-min rest after each charge. Notably, there is a significant rapid increase in EOCV observed after 250 cycles in cells treated with 15% LA (D6) and during initial cycling in cells without any LA (D3), highlighting more pronounced degradation mechanisms as cycling continues. Figure 4c showcases the CBC dV/dt signatures, which are prominently observed in the initial stages of cycling, notably as early as cycle 4 (dV/dt peaks), particularly in D3 cells. This pattern corresponds closely with the EOCV trends, unlike other designs where such dV/dt signatures are less evident. Supplemental Figure S 7b,c,d,e provides a detailed breakdown of CBC dV/dt signatures for Designs D3-D6 for various cycle numbers.

Figure 5 provides additional insights into the battery's performance through RPT data. This figure shows the average capacity fade and standard deviation measured at C/20 across various RPTs with respect to cycle number. There are clear, distinct patterns in capacity fade across the different cell designs. Cells without LA (D3) exhibit an accelerated capacity fade early in the cycling process, which later stabilizes to a slower rate of decline. In contrast, cells with 15% LA (D6) initially display a capacity fade rate similar to those with 9% (D4) and 12% LA (D5) up to 250 cycles. Beyond this point, however, the 15% LA cells begin to fade at a significantly faster rate, diverging sharply from the pattern observed in the 0% LA condition (D3) and culminating in over a 30% reduction by the 800th cycle, likely due to differing aging mechanisms. The poor performance of the 15% LA (D6) cells is attributed to LLI and loss of active material (LAM) in both NE and PE, as detailed in Section 3.4. Meanwhile, the 9% and 12% LA conditions demonstrate a more uniform, nearly linear aging trend, resulting in final capacity fades of 17.4% and 13.8% after 800 fast-charge cycles, respectively.

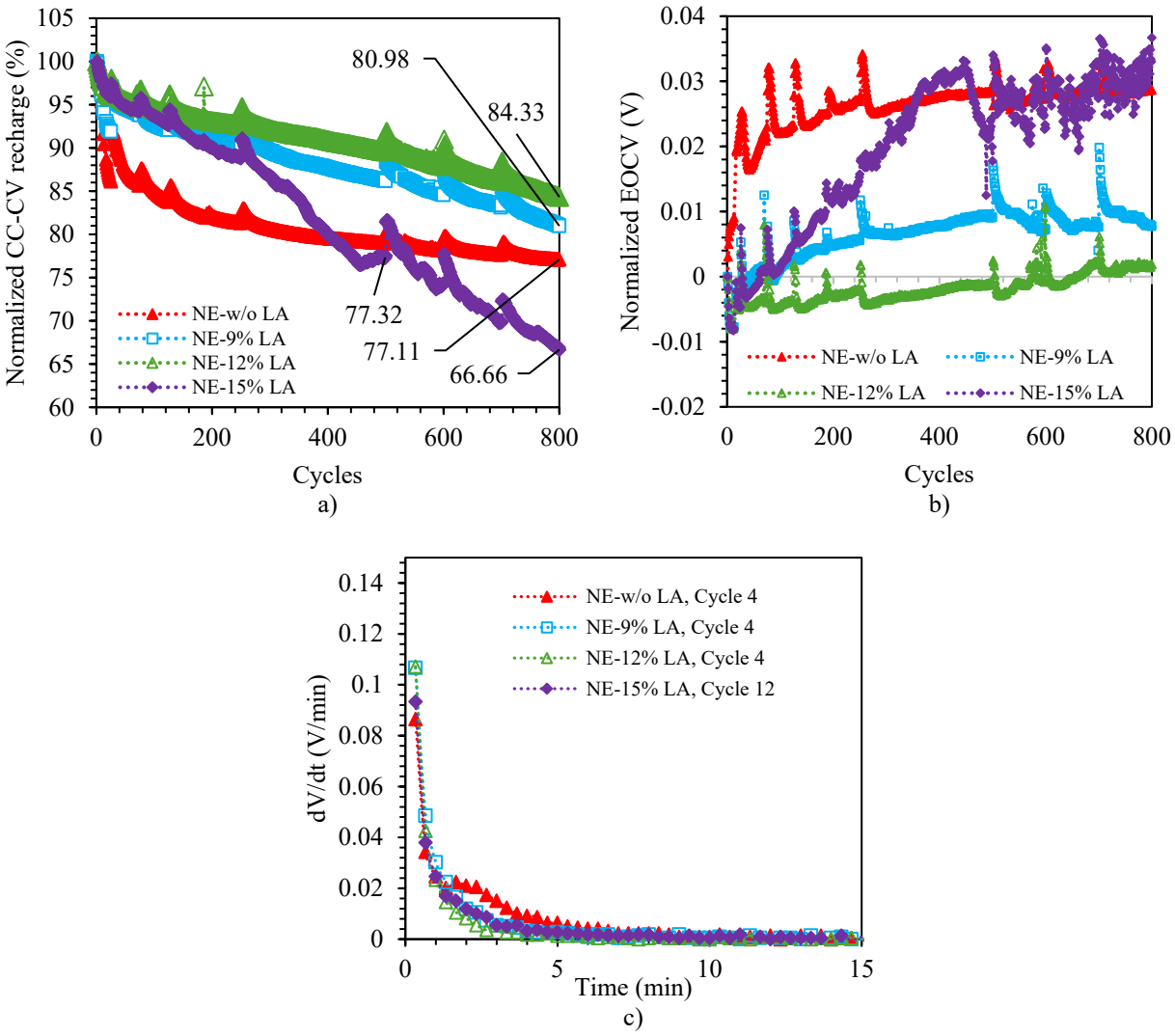

Figure 4. a) normalized CC-CV charge acceptance in 9%,12%,15% LA compared to BOL in %, b) EOCV curves for NE-9%, 12%, 15% LA compared to baseline NW-w/o LA, c) dV/dt curves for NE-9%,12%,15% LA compared to baseline NW-w/o LA. Note: Normalization was with respect to initial values at cycle 1.

The EIS curves in Figure S 7f, Figure 5b and c compare impedance at the BOL and at subsequent RPTs at 250 and 800 cycles, respectively. While improvements in impedance with varying percentages of LA remain inconclusive from these readings, a modest increase in impedance from BOL to 800 cycles is evident across all cell designs.

In summary, electrochemical analyses from Figure 4, Figure 5, and Figure S 7 reveal that Li-plating was a significant issue for cells treated with 15% LA (D6) and those without any LA (D3), as indicated by the severe C/20 capacity fade, EOCV, and dV/dt curves. In contrast, cells with 9% (D4) and 12% LA (D5) treatments exhibited much lower capacity fades of 17.4% and 13.8%, respectively, effectively avoiding Li-plating. To provide further clarity, we have included the C/20 capacity fade cycling data for each cell with D4, D5, D6 design treatments in Supplementary S5 (Figure S8). This comparative analysis underscores the effectiveness of moderate LA treatments in enhancing the resilience and longevity of cells under high-rate charging conditions

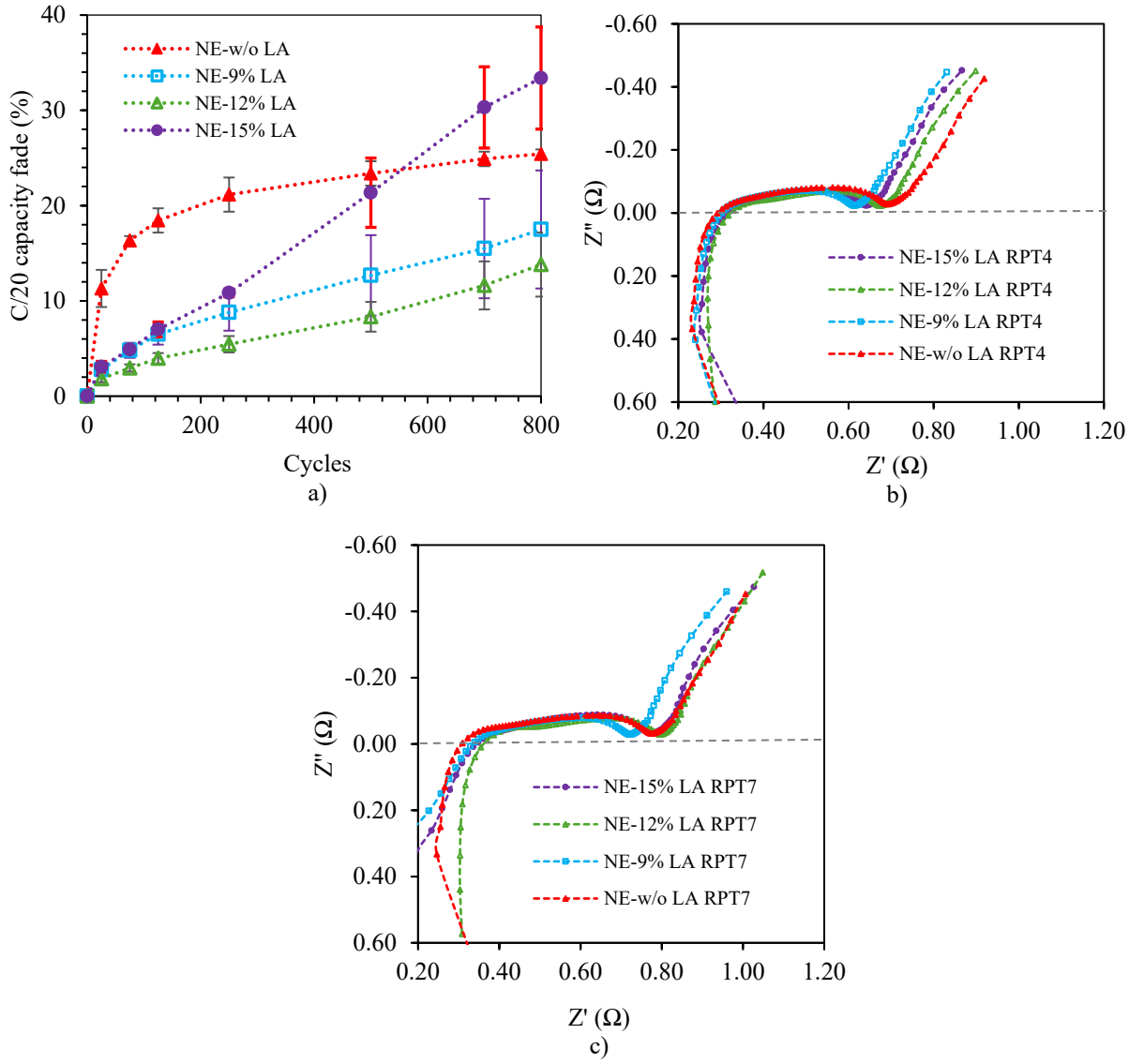

Figure 5. a) C/20 capacity fade data, Evolution of EIS curves for NE-9%,12%,15% LA compared to baseline NW-w/o LA at , b) RPT 4 (cycle 250) and c) RPT 7 (cycle 800)

3.4 Dominating Aging Modes

Understanding the dominant aging modes is crucial for design iterations in XFC. Earlier studies using the same materials and similar cell designs have indicated two primary aging modes: LLI and LAM in the positive electrode (LAMPE) [16,45,47,50–52]. In one previous study, LAM in the NE was identified. Upon diagnosis, the underlying issue was found to be the insufficient use of binder in the NE [8,17]. After re-optimization, the LAM in the NE no longer persisted [4]. As a

continuation of previous efforts, incremental capacity (IC) analysis was used here to identify the significant aging modes of these cell builds.

The average of the voltage and dQ/dV (C/20 basis) data from cells in each design (D3-D6) was used to examine IC. Then, the IC curves were plotted against voltage for the designs D3-D6 (Figure 6) at different RPTs (black curve at BOL, violet curve after 800 cycles). Significant dQ/dV peaks are associated with particular phase transitions in the graphite and NMC electrodes. The convolution of the graphite and NMC contributions is responsible for the three major peaks in Figure 6a, designated I, II, and III [45]. Peak I is associated with the lithiation and de-lithiation processes in graphite during charging and discharging, according to previous studies, whereas peaks II and III are associated with phase shifts in NMC that take place between 3.6 and 3.9V [53,54].

Capacity fading in commercial cell testing, which is mostly related to LLI, frequently stays consistent in the early stages. LLI arises from several factors: 1. Solid electrolyte interface (SEI) layer formation, 2. irreversible Li-plating, and 3. passivation of the positive electrode [55]. As shown in Figure 6a, the D3 exhibits a shift of peak I from 3.42V to 3.52V after 800 cycles (violet curve), along with a gradual decrease in peak II and a broadening and leftward shift of peak III. Previous reports have indicated that the non-uniform reduction and shifting of peaks are associated with LLI confirming that the design D3 experiences LLI [45,56]. This conclusion is further supported by EOCV, dV/dt (Figure 4b,c) and CBC data analysis (Figure 5, Figure S 7), suggesting that the LLI is likely due to Li-plating on the NE. Postmortem analysis after 800 cycles confirms these findings, indicating extensive Li-plating on the graphite surface, which interacts with the electrolyte to form a secondary SEI layer that worsens LLI [52,56]. The scenario involving D3 parallels the findings observed in the D4, D5, and D6 cases, where peak shifting and reduction were noted. This suggests that the cells under these conditions also experience LLI. Unlike the D3, peak I shifted to 3.49V and 3.48V for the D4, and D5, respectively (Figure 6b, c), with peak II showing a smaller reduction, indicating less LLI in the D5 case. Notably, a significant shift (from 3.42V to 3.54V) and reduction of peak I were observed in the D6 case (Figure 6d), confirming considerable LLI due to Li-plating. This finding aligns with EOCV(Figure 4b) and CBC data analyses (Figure 5, Figure S 7).

The second mode of aging involves LAM, which can happen in either the NE or PE. Figure 6a shows that peak I retains its intensity after 800 cycles (violet curve). Dubarry et al. suggested that gradual changes in peak intensity correspond to LAM [56]. The notable intensity change in peak II indicates LAM in the PE, as this peak is associated with NMC phase transitions. Additionally, the broadening of peak III (Figure 6a) suggests an increasing N/P ratio [53] confirming LAM in the PE for D3. Meanwhile, peak III consistently shifts to lower voltages across all configurations, indicating increased ohmic resistance. This shift is observed across configurations, although increased ohmic resistance mainly affects cell voltage rather than capacity [56]. In the D4 and D5 configurations, peak II remains visible even after 800 cycles. In contrast, peak II has completely disappeared in the configurations D3 and D6, indicating more LAM at the PE in these cases as compared to the D4 and D5 configurations. Similar to D3, peak III in D6 broadens and shifts to lower voltages due to increased ohmic resistance after 800 cycles.

Interestingly, in the D6 condition, peak I shows significant reduction after cycling. Since peak I corresponds to the lithiation and de-lithiation of graphite, this condition suggests LAM in the NE [53,54]. Additionally, the postmortem analysis after 800 cycles confirmed that microcracks and significant Li-plating occurred on the NE (Figure 7d,h). The microcrack observed on the NE reduces electronic conductivity, which may result in a decline in capacity. Furthermore, Li-plating on the laser-ablated region obstructs the interaction between the electrolyte and the anode materials (Figure 7h). The physical degradation of the NE, along with the increased Li-plating in the D6 cases, contributes to LAM/Li accumulation in the NE due to pore blockage [12]. Moreover, the LAM at the NE may contribute to reduced N/P capacity ratio, which impacts the charge-discharge cycling of the batteries [45]. The reduction and disappearance of peak II implies that LAM also occurs in the PE [53,54]. As a result, higher capacity fades happened for the D6 cases as compared to the other laser-ablated conditions. Therefore, in the D6, LLI occurred at the initial stage and then LAM impacts both the NE and PE.

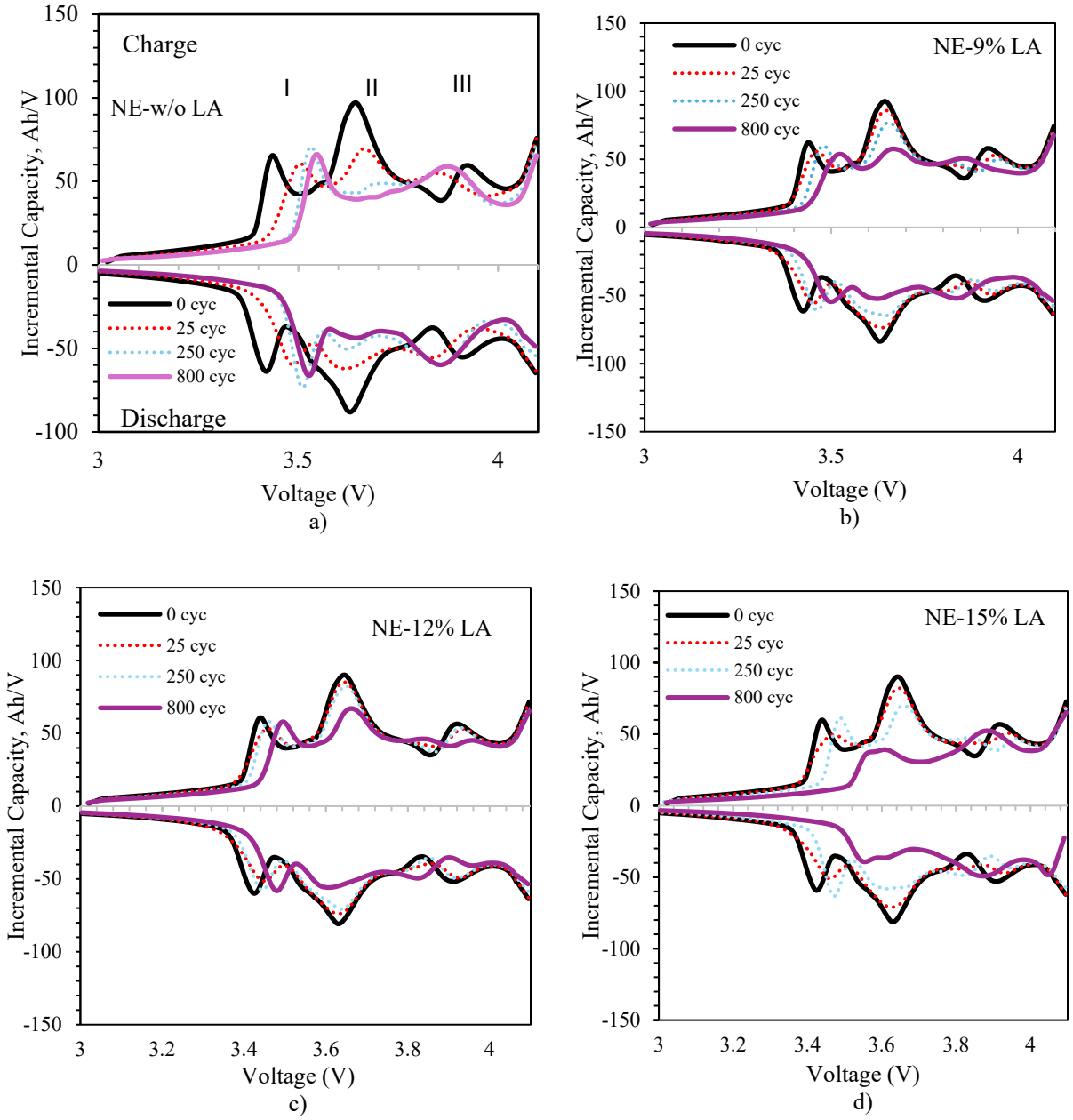

Figure 6. Incremental capacity, dQ/dV curves for a) NE- w/o LA, b) NE-9% LA, c) NE-12% LA, and d) NE-15% LA

3.5 Post-Mortem Characterization

3.5.1 Optical Images

In this investigation, we examined Li-plating occurrences in LiBs during fast-charge conditions by conducting post-mortem analyses on four cells. Each cell was subjected to an 800-cycle regimen at 5C-4.1V, represented in designs D3-D6, as depicted in Figure 7a-d. Prior to disassembly, the cells were discharged to 3V at C/3, followed by a 2-hr CV hold.

Optical imaging of the NE surfaces of the non-ablated (D3, Figure 7a) and 9% LA (D4, Figure 7b) revealed substantial Li deposits, identified by their shiny appearance, indicating significant Li-plating on the graphite NEs. The 15% LA design (D6, Figure 7d) also showed Li deposits. However, the Li deposits in the D6 were less pronounced than those in the D3 and D4 design cells. and higher than those realized in the D5 case. These observations align with the capacity degradation and Li-plating signatures outlined in Figure 4 and Figure 5, where designs D3, D4, and D6 exhibited capacity reductions of 25%, 17%, and 33%, respectively. Pore obstruction resulting from the significant amount of Li-plating was noted in the scenario involving D6 case, refer to Figure 7h. According to the IC analysis, the notable alteration in Peak II validated the presence of LAM at the PE (Section 3.4). In contrast, minimal Li deposits were observed in the D5 case (Figure 7c), correlating with the lower capacity fade of 13% noted in these cells. Although no electrochemical signatures of Li-plating were evident in earlier analyses from Figure 4, Figure 5, and Figure S 7, post-mortem examinations showed small amounts of Li-plating (Figure 7c). This supports the aging analysis from Section 3.4 (Figure 6c), indicating a minor degree of LLI in the D5 case. While Li-plating is evident from various data sources discussed herein, the “shiny” artifacts in optical images may not provide accurate quantification of this mechanism, as some of the surface anomalies noted in Figure 7a-d could also be salt residue or other SEI remnants that accumulated on the anode surfaces.

These findings align with the detailed analysis in Section 3.4 of the dQ/dV profiles, which demonstrated significant reductions in peaks I, II, and III, pinpointing LLI as the primary cause of the observed capacity fade. Furthermore, the results support existing studies indicating that Li-plating typically becomes irreversible at high C-rates above 3C [49,57]. This irreversible deposition was evident in the analysis of cells subjected to a 5C-4.1V charging regimen, particularly in cells from designs D3, D4, and D6, as illustrated in Figure 7 a, b, and d. The study also confirmed that all cells were discharged to 3V at C/3 followed by a 2-hr CV hold before disassembly, further validating the identification of irreversible Li-plating.

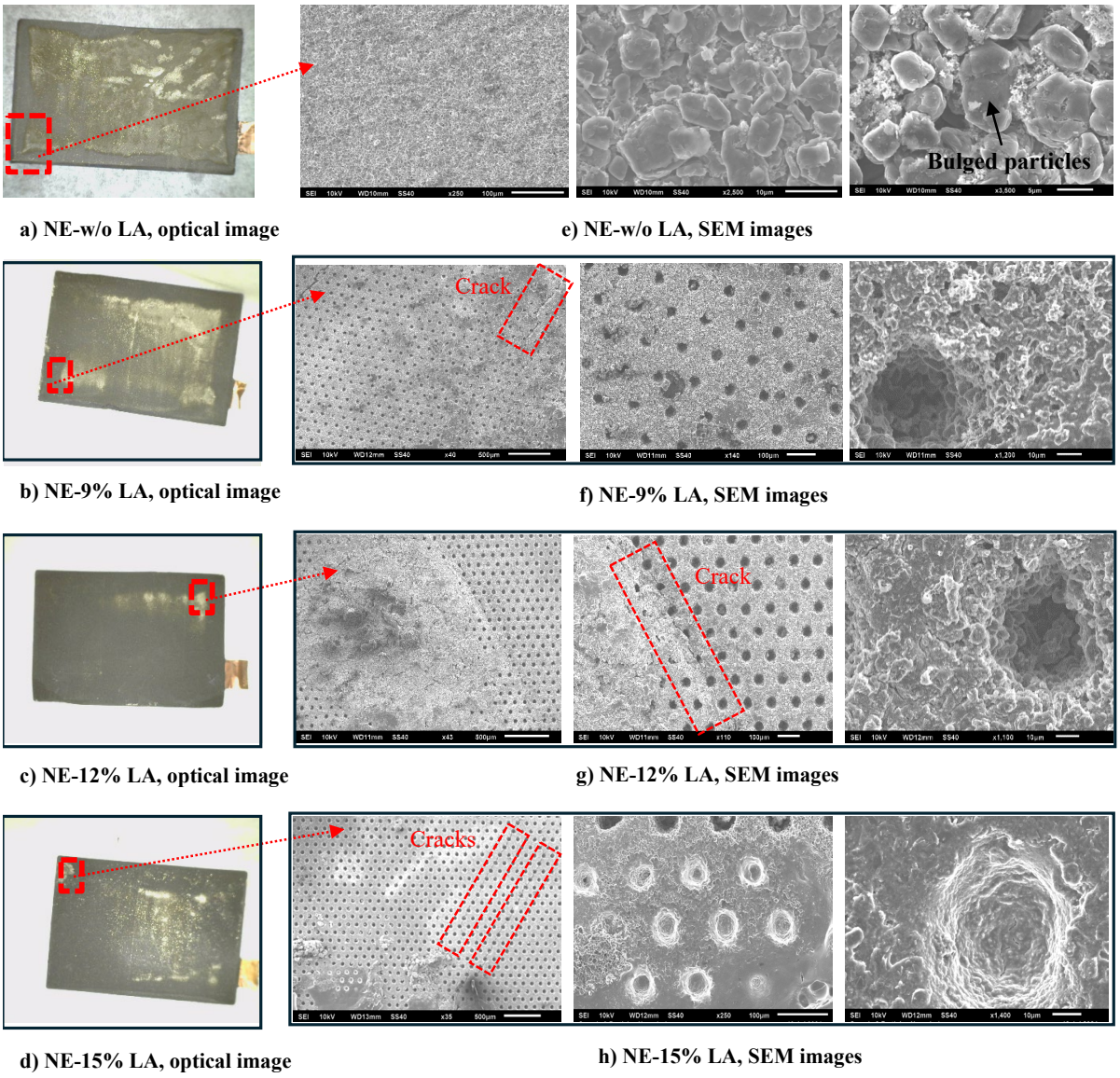

a) NE-w/o LA, optical image

e) NE-w/o LA, SEM images

b) NE-9% LA, optical image

f) NE-9% LA, SEM images

c) NE-12% LA, optical image

g) NE-12% LA, SEM images

d) NE-15% LA, optical image

h) NE-15% LA, SEM images

Figure 7. Optical images of NE after 800 cycles: a) NE- w/o LA, b) NE-9% LA, c) NE-12% LA, d) NE-15% LA, and SEM images of NE after 800 cycles: e) NE- w/o LA, f) NE-9% LA, g) NE-12% LA, and h) NE-15% LA

3.5.2 SEM Imaging

In this study, SEM images of both pristine and cycled NE samples are analyzed and shown in Figure 8 and Figure 7, respectively. Figure 7e features D3 cell, where shiny areas are indicative of Li-plating and bulged particles are evident as compared to the pristine NE shown in Figure 8a [58]. This suggests that a significant portion of the capacity fade of 25% was primarily due to extensive Li-plating. Similarly, the D6 cell (Figure 7h) shows a higher capacity fade of 33%, which can be attributed to residues that include Li deposits and Li-plating on the NE [58,59]. Li-plating was also detected within the ablated holes, exacerbating the degradation on the anode materials and causes higher LLI. It is recognized that quantification of Li-plating would require additional chemical analyses of the harvested anodes, and that the shiny artifacts might not be strictly due to Li deposition on the surface.

In contrast, D4 (Figure 7f) and D5 (Figure 7g) cells displayed no dendritic structures, although some electrolyte salt residue may be present. Notably, D4 cells (Figure 7f) experienced a reduction in hole size due to plating, whereas the D5 cells (Figure 7g) preserved the uniformity of the laser-ablated holes even after 800 fast charge cycles, demonstrating negligible Li-plating. Moreover, across all cells with LA, we noticed cracking along the electrode at the ablated holes, suggesting that the LA process might be influencing these structural changes. For D6 electrodes, SEM analysis of the fresh electrode reveals no microcracks, indicating that such microcracks develop during cycling. Consistent capacity fading was observed up to 250 cycles, but a significant capacity decline after 250 cycles suggests structural changes occur due to cycling. Notably, the pore diameter of the 12% LA samples is larger than that of other LA samples (Figure S 3e), and this case exhibits better performance. Therefore, it can be concluded that the pore size and the distance between the pores greatly influence the structural strength of the electrode.

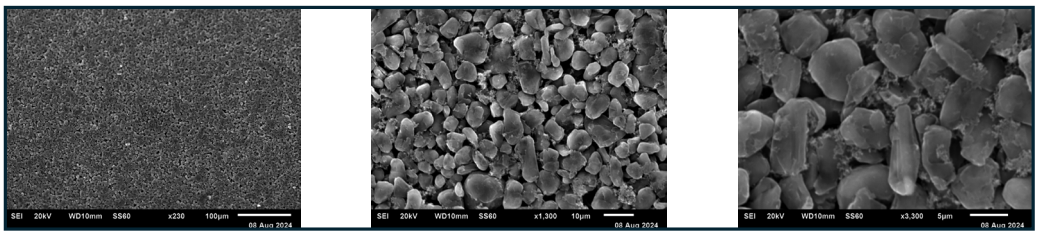

a) NE-w/o LA

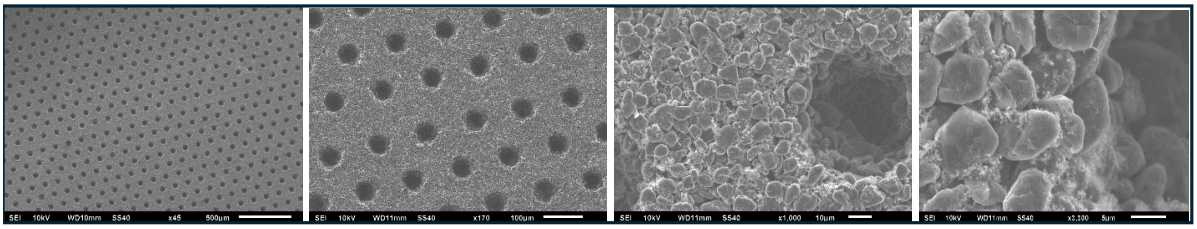

b) NE-9% LA

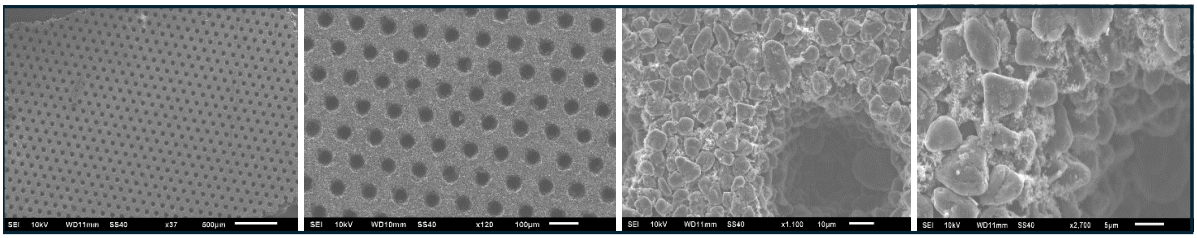

c) NE-12% LA

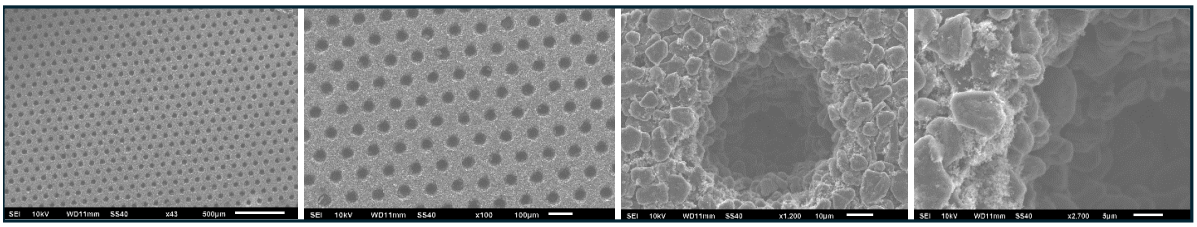

d) NE-15% LA

Figure 8. Pristine NE SEM images for a) NE- w/o LA, b) NE-9% LA, c) NE-12% LA, and d) NE-15% LA

4 Discussion

The work presented in this manuscript highlights the role of conductive additives in enhancing the XFC performance of high-loading electrodes. Integrating SWCNTs into the NMC PE has proven to markedly enhance electrical conductivity and charge acceptance, which are critical during fast-charge conditions. SWCNTs not only reduces impedance (Figure 2a) but also prevents the development of plateaus in transport polarization (Figure 2b) and peaks in dV/dt curves (Figure S 4b), effectively suppressing Li-plating. This adaptation results in a notable increase in charge acceptance by 13.1% at a 5C rate within a 3-4.1V window (Figure S 4d), highlighting the considerable advantages of SWCNTs in enhancing the performance of high-loading cell designs.

LA in the NE can further improve electrode/cell polarization, as detailed in NREL's previous study [32]. This comprehensive study, through modeling and experiments, demonstrated the benefits of LA in enhancing cell transport potential. However, optimizing LA is necessary to maximize the benefits observed in this study. Further enhancements have been achieved through the strategic combination of SWCNTs (in the PE) with LA in the NE (D4-D6). This synergy has resulted in up to a 40% improvement in transport polarization (Figure S 6a) and charge acceptance rates reaching as high as 85% at 5C (Figure 3d). Such dual modifications not only exhibit synergistic effects but also set new performance benchmarks, significantly extending the operational efficiency and cycle life under demanding conditions.

Cycle-life analysis further demonstrated the durability of these enhancements. Moderate levels of LA (9% and 12%) effectively minimized capacity fade, showing capacity fades of only 17% and 13% respectively after 800 fast-charge cycles. In contrast, cells with a higher degree of ablation (15%) showed considerable capacity reduction and severe Li-plating, evidenced by EOCV (Figure 4b), dV/dt (Figure 4c), C/20 capacity fade (Figure 5a), and optical/SEM analyses (Figure 7a-h). These issues underscore the need for optimal LA to prevent excessive LLI. dQ/dV analysis supports these observations, highlighting increased LLI and LAM in cells with no LA and those with the highest ablation level (15% LA).

Regarding aging modes, the study identifies that LAM, whether in NE or PE, presents significant challenges, particularly under high operational demands such as XFC. The analysis of peak shifts in dQ/dV profiles, such as the notable reduction in peak I for cells with 15% LA (Figure 6d), directly ties to extensive LLI and LAM in the NE, further supported by postmortem analysis showing extensive Li-plating and physical degradation. The deterioration of the negative electrode, resulting from microcracks and Li-plating, results in LAM at the NE. Consequently, this diminishes the battery's performance at high C-rate. These observations suggest that while LA and SWCNTs provide substantial benefits, their impacts on aging modes must be carefully balanced to optimize battery health and ensure the viability of LiBs for future high-performance applications.

In the ongoing exploration of strategies to enable extreme fast charging within 10-15 mins, it's evident from the findings reported in article [4] that there is no singular solution or design that can achieve this objective alone. Instead, a multifaceted approach is required. Previously, six different strategies were evaluated: optimizing PE chemistry, enhancing the carbon binder domain in the PE, implementing dual layer NE designs, utilizing high porosity separators, employing advanced

electrolytes, and developing innovative charging protocols [4,23]. In the present study, we have added two additional strategies—integrating SWCNTs into the PE and applying LA to the NE—even without leveraging advanced charging protocols.

The integration of these strategies has demonstrated significant improvements in battery performance, underscoring the potential for a combined approach to meet the demands of XFC. It is reasonable to anticipate that by selecting and synergizing the most effective solution strategies, particularly in energy-optimized cells with higher active material loadings (~4 mAh cm^{-2}), it is possible to successfully achieve the goal of 10–15 min fast charging. Such an approach would not only push the boundaries of current battery technology but also significantly enhance the practical usability and adoption of electric vehicles.

5 Conclusion

This study underscores the effectiveness of incorporating Single-Wall Carbon Nanotubes (SWCNTs) and Laser Ablation (LA) into the positive electrode (PE) and negative electrode (NE) of LiBs, respectively, aiming to achieve rapid charging capabilities within the ambitious 10-15 min timeframe. The findings illustrate that augmenting cells with SWCNTs in the PE significantly enhances charge acceptance, showing a 13.1% increase at 5C rates, and effectively mitigates issues related to cell polarization. This positions SWCNT-enhanced cells as highly viable for demanding fast charging applications. Additionally, employing moderate levels of LA (9% and 12%) in the NE not only preserves the battery's capacity over 800 cycles—demonstrating capacity fade of merely 17.4 % and 13.8 %, respectively—but also prevents the negative impacts associated with high-rate charging. Conversely, higher levels of LA (15%) introduce more significant capacity losses and Li-plating, highlighting the need to carefully balanced LA amounts and aging-informed cell-balancing to optimize performance and avoid detrimental effects such as LLI.

By adopting a 5C (12-min) charging protocol, cycling-performance data validates the combined benefits of SWCNTs in the PE and LA in the NE in high-loading cells and elucidate their long-term impacts on battery performance. A methodological in situ and post-mortem approach is used to identify key aging mechanisms. This analysis shows that moderate levels of LA in the negative electrode are indeed a feasible strategy for enabling XFC without incurring significant long-term issues.

The combined implementation of these technologies represents a substantial advancement in LiB development. This integrated approach not only reduces the risk of Li-plating but also establishes a foundation for further innovations in battery technology.

6 Appendix

List of all Abbreviations

BOL	Beginning-of-life
CC-CV	Constant current constant voltage
CE	Coulombic efficiency
C-rate	Charging rate
DiffCap	Differential capacity
dQ/dV	Differential IC
dV/dt	Differential voltage wrt time
EIS	Electrochemical impedance spectroscopy
EOCV	End of charge rest voltage
FCC	Fast charge capability
Gr	Graphite
HPPC	Hybrid pulse-power characterization
IC	Incremental capacity
LA	Laser ablation
LAM	Loss of active material
LiB	Lithium-ion batteries
LLI	Loss of Li inventory
NE	Negative electrode
OCV	Open circuit voltage
PE	Positive electrode
RCT	Rate capability test
RPT	Reference performance tests
SEI	Solid electrolyte interface
SEM	Scanning electron microscope
SWCNT	Single-walled carbon nano tubes

Acknowledgement

The authors thank Jake Herb from DOE for supporting this project. Funding was provided by the DOE Office of Energy Efficiency and Renewable Energy's Vehicle Technologies Office under the guidance of the Advanced Battery Cell Research XCEL Program. This manuscript was authored by Battelle Energy Alliance, LLC, under Contract No. DE-AC07-05ID14517 for INL; the Alliance for Sustainable Energy, LLC, under Contract No. DE-AC36-08GO28308 for NREL; and the University of Chicago–Argonne, LLC, under Contract No. DE-AC02-06CH11357 for Argonne, all of which are DOE-Office of Science Laboratories. This article has been contributed to by U.S. Government subcontractors and their work is in the public domain in the USA.

References

[1] N. Naughton, Electric Vehicles Are the U.S. Auto Industry's Future—if Dealers Can Figure Out How to Sell Them, (2021). https://www.wsj.com/articles/electric-vehicles-are-the-u-s-auto-industrys-futureif-dealers-can-figure-out-how-to-sell-them-11615113000 (accessed February 26, 2024).

[2] P. Verma, Soon electric vehicles could charge faster than your iPhone, (2022). https://www.washingtonpost.com/technology/2022/08/27/electric-vehicle-charge-time/ (accessed February 26, 2024).

[3] S. Ahmed, I. Bloom, A.N. Jansen, T. Tanim, E.J. Dufek, A. Pesaran, A. Burnham, R.B. Carlson, F. Dias, K. Hardy, M. Keyser, C. Kreuzer, A. Markel, A. Meintz, C. Michelbacher, M. Mohanpurkar, P.A. Nelson, D.C. Robertson, D. Scoffield, M. Shirk, T. Stephens, R. Vijayagopal, J. Zhang, Enabling fast charging – A battery technology gap assessment, J. Power Sources 367 (2017) 250–262. https://doi.org/10.1016/j.jpowsour.2017.06.055.

[4] T.R. Tanim, S. Kim, A.M. Colclasure, Z. Yang, K. Gering, P.J. Weddle, M. Evans, E.J. Dufek, Y. Lin, J. Wen, F. Usseglio-Viretta, A.R. Dunlop, S.E. Trask, K. Smith, B.J. Ingram, A.N. Jansen, Rational designs to enable 10-min fast charging and long cycle life in lithium-ion batteries, J. Power Sources 582 (2023) 233519. https://doi.org/10.1016/j.jpowsour.2023.233519.

[5] T.R. Tanim, P.P. Paul, V. Thampy, C. Cao, H.-G. Steinrück, J. Nelson Weker, M.F. Toney, E.J. Dufek, M.C. Evans, A.N. Jansen, B.J. Polzin, A.R. Dunlop, S.E. Trask, Heterogeneous Behavior of Lithium Plating during Extreme Fast Charging, Cell Rep. Phys. Sci. 1 (2020) 100114. https://doi.org/10.1016/j.xcrp.2020.100114.

[6] E.J. Dufek, D.P. Abraham, I. Bloom, B.-R. Chen, P.R. Chinnam, A.M. Colclasure, K.L. Gering, M. Keyser, S. Kim, W. Mai, D.C. Robertson, M.-T.F. Rodrigues, K. Smith, T.R. Tanim, F.L.E. Usseglio-Viretta, P.J. Weddle, Developing extreme fast charge battery protocols – A review spanning materials to systems, J. Power Sources 526 (2022) 231129. https://doi.org/10.1016/j.jpowsour.2022.231129.

[7] A. Adam, J. Wandt, E. Knobbe, G. Bauer, A. Kwade, Fast-Charging of Automotive Lithium-Ion Cells: In-Situ Lithium-Plating Detection and Comparison of Different Cell Designs, J. Electrochem. Soc. 167 (2020) 130503. https://doi.org/10.1149/1945-7111/abb564.

[8] T.R. Tanim, P.J. Weddle, Z. Yang, A.M. Colclasure, H. Charalambous, D.P. Finegan, Y. Lu, M. Preefer, S. Kim, J.M. Allen, Enabling Extreme Fast-Charging: Challenges at the Cathode and Mitigation Strategies, Adv. Energy Mater. 12 (2022) 2202795.

[9] E.J. McShane, P.P. Paul, T.R. Tanim, C. Cao, H.-G. Steinrück, V. Thampy, S.E. Trask, A.R. Dunlop, A.N. Jansen, E.J. Dufek, Multimodal quantification of degradation pathways during extreme fast charging of lithium-ion batteries, J. Mater. Chem. A 10 (2022) 23927–23939.

[10] P.R. Chinnam, A.M. Colclasure, B.-R. Chen, T.R. Tanim, E.J. Dufek, K. Smith, M.C. Evans, A.R. Dunlop, S.E. Trask, B.J. Polzin, A.N. Jansen, Fast-Charging Aging Considerations: Incorporation and Alignment of Cell Design and Material Degradation Pathways, ACS Appl. Energy Mater. 4 (2021) 9133–9143. https://doi.org/10.1021/acsaem.1c01398.

[11] A. Laforgue, X.-Z. Yuan, A. Platt, S. Brueckner, F. Perrin-Sarazin, M. Toupin, J.-Y. Huot, A. Mokrini, Effects of fast charging at low temperature on a high energy Li-ion battery, J. Electrochem. Soc. 167 (2020) 140521.

[12] P.P. Paul, V. Thampy, C. Cao, H.-G. Steinrück, T.R. Tanim, A.R. Dunlop, E.J. Dufek, S.E. Trask, A.N. Jansen, M.F. Toney, Quantification of heterogeneous, irreversible lithium plating in extreme fast charging of lithium-ion batteries, Energy Environ. Sci. 14 (2021) 4979–4988.

[13] M. Yusuf, J.M. LaManna, P.P. Paul, D.N. Agyeman-Budu, C. Cao, A.R. Dunlop, A.N. Jansen, B.J. Polzin, S.E. Trask, T.R. Tanim, Simultaneous neutron and X-ray tomography for visualization of graphite electrode degradation in fast-charged lithium-ion batteries, Cell Rep. Phys. Sci. 3 (2022).

[14] A.M. Colclasure, T.R. Tanim, A.N. Jansen, S.E. Trask, A.R. Dunlop, B.J. Polzin, I. Bloom, D. Robertson, L. Flores, M. Evans, E.J. Dufek, K. Smith, Electrode scale and electrolyte transport effects on extreme fast charging of lithium-ion cells, Electrochimica Acta 337 (2020) 135854. https://doi.org/10.1016/j.electacta.2020.135854.

[15] T.R. Tanim, Z. Yang, D.P. Finegan, P.R. Chinnam, Y. Lin, P.J. Weddle, I. Bloom, A.M. Colclasure, E.J. Dufek, J. Wen, A comprehensive understanding of the aging effects of extreme fast charging on high Ni NMC cathode, Adv. Energy Mater. 12 (2022) 2103712.

[16] T.R. Tanim, Z. Yang, A.M. Colclasure, P.R. Chinnam, P. Gasper, Y. Lin, L. Yu, P.J. Weddle, J. Wen, E.J. Dufek, Extended cycle life implications of fast charging for lithium-ion battery cathode, Energy Storage Mater. 41 (2021) 656–666.

[17] F.L. Usseglio-Viretta, A.M. Colclasure, A.R. Dunlop, S.E. Trask, A.N. Jansen, D.P. Abraham, M.-T.F. Rodrigues, E.J. Dufek, T.R. Tanim, P.R. Chinnam, Carbon-Binder Weight Loading Optimization for Improved Lithium-Ion Battery Rate Capability, J. Electrochem. Soc. 169 (2022) 070519.

[18] J.E. Harlow, X. Ma, J. Li, E. Logan, Y. Liu, N. Zhang, L. Ma, S.L. Glazier, M.M. Cormier, M. Genovese, A wide range of testing results on an excellent lithium-ion cell chemistry to be used as benchmarks for new battery technologies, J. Electrochem. Soc. 166 (2019) A3031.

[19] X. Ma, R.S. Arumugam, L. Ma, E. Logan, E. Tonita, J. Xia, R. Petibon, S. Kohn, J. Dahn, A study of three ester co-solvents in lithium-ion cells, J. Electrochem. Soc. 164 (2017) A3556.

[20] X. Ma, J. Li, S.L. Glazier, L. Ma, K.L. Gering, J. Dahn, A study of highly conductive ester co-solvents in Li [Ni0. 5Mn0. 3Co0. 2] O2/Graphite pouch cells, Electrochimica Acta 270 (2018) 215–223.

[21] D.S. Hall, A. Eldesoky, E. Logan, E.M. Tonita, X. Ma, J. Dahn, Exploring classes of co-solvents for fast-charging lithium-ion cells, J. Electrochem. Soc. 165 (2018) A2365.

[22] E. Logan, E.M. Tonita, K. Gering, J. Li, X. Ma, L. Beaulieu, J. Dahn, A study of the physical properties of Li-ion battery electrolytes containing esters, J. Electrochem. Soc. 165 (2018) A21.

[23] N. Gao, S. Kim, P. Chinnam, E.J. Dufek, A.M. Colclasure, A. Jansen, S.-B. Son, I. Bloom, A. Dunlop, S. Trask, K.L. Gering, Methodologies for design, characterization and testing of electrolytes that enable extreme fast charging of lithium-ion cells, Energy Storage Mater. 44 (2022) 296–312.

[24] Z. Du, D.L. Wood III, I. Belharouak, Enabling fast charging of high energy density Li-ion cells with high lithium ion transport electrolytes, Electrochem. Commun. 103 (2019) 109–113.

[25] I.A. Shkrob, M.-T.F. Rodrigues, D.W. Dees, D.P. Abraham, Fast charging of Li-ion cells: Part II. nonlinear contributions to cell and electrode polarization, J. Electrochem. Soc. 166 (2019) A3305.

[26] A. Abdulhameed, N.Z.A. Wahab, M.N. Mohtar, M.N. Hamidon, S. Shafie, I.A. Halin, Methods and Applications of Electrical Conductivity Enhancement of Materials Using Carbon Nanotubes, J. Electron. Mater. 50 (2021) 3207–3221. https://doi.org/10.1007/s11664-021-08928-2.

[27] J.H. Choi, C. Lee, S. Park, M. Hwang, T.J. Embleton, K. Ko, M. Jo, K.S. Saqib, J. Yun, M. Jo, Y. Son, P. Oh, Improved electrochemical performance using well-dispersed carbon nanotubes as conductive additive in the Ni-rich positive electrode of lithium-ion batteries, Electrochem. Commun. 146 (2023) 107419. https://doi.org/10.1016/j.elecom.2022.107419.

[28] H. Kim, J.H. Lim, T. Lee, J. An, H. Kim, H. Song, H. Lee, J.W. Choi, J.H. Kang, Ozone-Treated Carbon Nanotube as a Conductive Agent for Dry-Processed Lithium-Ion Battery Cathode, ACS Energy Lett. 8 (2023) 3460–3466.

[29] S. Zhong, H. Liu, D. Wei, J. Hu, H. Zhang, H. Hou, M. Peng, G. Zhang, H. Duan, Long-aspect-ratio N-rich carbon nanotubes as anode material for sodium and lithium ion batteries, Chem. Eng. J. 395 (2020) 125054. https://doi.org/10.1016/j.cej.2020.125054.

[30] I.A. Kinloch, J. Suhr, J. Lou, R.J. Young, P.M. Ajayan, Composites with carbon nanotubes and graphene: An outlook, Science 362 (2018) 547–553.

[31] M. Firoozan, M. Baniassadi, M. Baghani, A. Chortos, In silico optimization of aligned fiber electrodes for dielectric elastomer actuators, Sci. Rep. 14 (2024) 1–11.

[32] N. Dunlap, D.B. Sulas-Kern, P.J. Weddle, F. Usseglio-Viretta, P. Walker, P. Todd, D. Boone, A.M. Colclasure, K. Smith, B.J.T. de Villers, Laser ablation for structuring Li-ion electrodes for fast charging and its impact on material properties, rate capability, Li plating, and wetting, J. Power Sources 537 (2022) 231464.

[33] J. Kriegler, L. Hille, S. Stock, L. Kraft, J. Hagemeister, J.B. Habedank, A. Jossen, M.F. Zaeh, Enhanced performance and lifetime of lithium-ion batteries by laser structuring of graphite anodes, Appl. Energy 303 (2021) 117693.

[34] J.B. Habedank, F.J. Günter, N. Billot, R. Gilles, T. Neuwirth, G. Reinhart, M.F. Zaeh, Rapid electrolyte wetting of lithium-ion batteries containing laser structured electrodes: in situ visualization by neutron radiography, Int. J. Adv. Manuf. Technol. 102 (2019) 2769–2778.

[35] K.-H. Chen, M.J. Namkoong, V. Goel, C. Yang, S. Kazemiabnavi, S. Mortuza, E. Kazyak, J. Mazumder, K. Thornton, J. Sakamoto, Efficient fast-charging of lithium-ion batteries enabled by laser-patterned three-dimensional graphite anode architectures, J. Power Sources 471 (2020) 228475.

[36] J.B. Habedank, J. Kriegler, M.F. Zaeh, Enhanced fast charging and reduced lithium-plating by laser-structured anodes for lithium-ion batteries, J. Electrochem. Soc. 166 (2019) A3940.

[37] W. Pfleging, A review of laser electrode processing for development and manufacturing of lithium-ion batteries, 7 (2018) 549–573. https://doi.org/10.1515/nanoph-2017-0044.

[38] C.-Y. Wang, T. Liu, X.-G. Yang, S. Ge, N.V. Stanley, E.S. Rountree, Y. Leng, B.D. McCarthy, Fast charging of energy-dense lithium-ion batteries, Nature 611 (2022) 485–490.

[39] A. Babkin, A. Kubarkov, O. Drozhzhin, S. Urvanov, I. Filimonenkov, A. Tkachev, V. Mordkovich, V. Sergeyev, E. Antipov, Single-, double-, and multi-walled carbon nanotubes as electrically conductive additives to lithium-ion battery cathodes, in: Springer, 2023: pp. 1–9.

[40] P. Sehrawat, C. Julien, S.S. Islam, Carbon nanotubes in Li-ion batteries: A review, Li-Ion Batter. 213 (2016) 12–40. https://doi.org/10.1016/j.mseb.2016.06.013.

[41] A.M. Colclasure, A.R. Dunlop, S.E. Trask, B.J. Polzin, A.N. Jansen, K. Smith, Requirements for Enabling Extreme Fast Charging of High Energy Density Li-Ion Cells while Avoiding Lithium Plating, J. Electrochem. Soc. 166 (2019) A1412. https://doi.org/10.1149/2.0451908jes.

[42] COMSOL, 3D Electrochemical and Thermal Analysis of a Prismatic Lithium Battery, (n.d.). https://www.comsol.com/model/3d-electrochemical-and-thermal-analysis-of-a-prismatic-lithium-battery-124881.

[43] F.L.E. Usseglio-Viretta, P. Patel, E. Bernhardt, A. Mistry, P.P. Mukherjee, J. Allen, S.J. Cooper, J. Laurencin, K. Smith, MATBOX: An Open-source Microstructure Analysis Toolbox for microstructure generation, segmentation, characterization, visualization, correlation, and meshing, SoftwareX 17 (2022) 100915. https://doi.org/10.1016/j.softx.2021.100915.

[44] K. Gering, AEM: Molecular-Based Battery Electrolyte Optimization and Analysis, (n.d.). https://inlsoftware.inl.gov/product/aem.

[45] T.R. Tanim, E.J. Dufek, M. Evans, C. Dickerson, A.N. Jansen, B.J. Polzin, A.R. Dunlop, S.E. Trask, R. Jackman, I. Bloom, Z. Yang, E. Lee, Extreme Fast Charge Challenges for Lithium-Ion Battery: Variability and Positive Electrode Issues, J. Electrochem. Soc. 166 (2019) A1926. https://doi.org/10.1149/2.0731910jes.

[46] J.P. Christophersen, Battery Test Manual For Electric Vehicles, Revision 3, (2015). https://doi.org/10.2172/1186745.

[47] B.-R. Chen, C.M. Walker, S. Kim, M.R. Kunz, T.R. Tanim, E.J. Dufek, Battery aging mode identification across NMC compositions and designs using machine learning, Joule 6 (2022) 2776–2793. https://doi.org/10.1016/j.joule.2022.10.016.

[48] B.-R. Chen, M.R. Kunz, T.R. Tanim, E.J. Dufek, A machine learning framework for early detection of lithium plating combining multiple physics-based electrochemical signatures, Cell Rep. Phys. Sci. 2 (2021) 100352. https://doi.org/10.1016/j.xcrp.2021.100352.

[49] G. Vennam, T.R. Tanim, J.T. Todd, L.K. Walker, Advancing Li-plating detection: Motivating a multi-signal correlation approach, J. Energy Storage 98 (2024) 112869.

[50] G. Vennam, B.-R. Chen, S. Kim, T.R. Tanim, The importance of cycle-by-cycle data in performing rapid battery technology development and validation, J. Energy Storage 95 (2024) 112579.

[51] S. Kim, Z. Yi, M.R. Kunz, E.J. Dufek, T.R. Tanim, B.-R. Chen, K.L. Gering, Accelerated battery life predictions through synergistic combination of physics-based models and machine learning, Cell Rep. Phys. Sci. 3 (2022) 101023. https://doi.org/10.1016/j.xcrp.2022.101023.

[52] T.R. Tanim, M.G. Shirk, R.L. Bewley, E.J. Dufek, B.Y. Liaw, Fast charge implications: Pack and cell analysis and comparison, J. Power Sources 381 (2018) 56–65. https://doi.org/10.1016/j.jpowsour.2018.01.091.

[53] C. Busà, M. Belekoukia, M.J. Loveridge, The effects of ambient storage conditions on the structural and electrochemical properties of NMC-811 cathodes for Li-ion batteries, Electrochimica Acta 366 (2021) 137358. https://doi.org/10.1016/j.electacta.2020.137358.

[54] R. Jung, M. Metzger, F. Maglia, C. Stinner, H.A. Gasteiger, Oxygen Release and Its Effect on the Cycling Stability of LiNixMnyCozO2 (NMC) Cathode Materials for Li-Ion Batteries, J. Electrochem. Soc. 164 (2017) A1361. https://doi.org/10.1149/2.0021707jes.

[55] L. Spitthoff, P.J.S. Vie, M.S. Wahl, J. Wind, O.S. Burheim, Incremental capacity analysis (dQ/dV) as a tool for analysing the effect of ambient temperature and mechanical clamping on degradation, J. Electroanal. Chem. 944 (2023) 117627. https://doi.org/10.1016/j.jelechem.2023.117627.

[56] M. Dubarry, C. Truchot, B.Y. Liaw, Synthesize battery degradation modes via a diagnostic and prognostic model, J. Power Sources 219 (2012) 204–216. https://doi.org/10.1016/j.jpowsour.2012.07.016.

[57] P.R. Chinnam, T.R. Tanim, E.J. Dufek, C.C. Dickerson, M. Li, Sensitivity and reliability of key electrochemical markers for detecting lithium plating during extreme fast charging, J. Energy Storage 46 (2022) 103782. https://doi.org/10.1016/j.est.2021.103782.

[58] G. Zhang, X. Wei, G. Han, H. Dai, J. Zhu, X. Wang, X. Tang, J. Ye, Lithium plating on the anode for lithium-ion batteries during long-term low temperature cycling, J. Power Sources 484 (2021) 229312. https://doi.org/10.1016/j.jpowsour.2020.229312.

[59] Q. Xu, J. Lin, C. Ye, X. Jin, D. Ye, Y. Lu, G. Zhou, Y. Qiu, W. Li, Air-stable and dendrite-free lithium metal anodes enabled by a hybrid interphase of C60 and Mg, Adv. Energy Mater. 10 (2020) 1903292.